



# Controlled fabrication and enhanced visible-light photocatalytic hydrogen production of Au@CdS/MIL-101 heterostructure

Yajun Wang<sup>a</sup>, Yunnuan Zhang<sup>a</sup>, Zhiqiang Jiang<sup>b</sup>, Guiyuan Jiang<sup>a,\*</sup>, Zhen Zhao<sup>a,\*</sup>, Qiaohuan Wu<sup>a</sup>, Ying Liu<sup>a</sup>, Quan Xu<sup>a</sup>, Aijun Duan<sup>a</sup>, Chunming Xu<sup>a</sup>

<sup>a</sup> State Key Laboratory of Heavy Oil Processing, China University of Petroleum Beijing, Beijing 102249, People's Republic of China

<sup>b</sup> Panzhuhua Key Laboratory of Chemical Resource Engineering, Panzhuhua University, Panzhuhua 617000, People's Republic of China

## ARTICLE INFO

### Article history:

Received 25 September 2015

Received in revised form

30 November 2015

Accepted 11 December 2015

Available online 17 December 2015

### Keywords:

CdS

MOFs

MIL-101

Au@CdS

Photocatalytic hydrogen production

## ABSTRACT

A novel and highly efficient three-component Au@CdS/MIL-101 heterostructure was successfully synthesized. The MIL-101(Cr) with large surface area was introduced as a matrix for the well-dispersed growth of Au nanoparticles, and the CdS was selectively coated on the Au nanoparticles. Under visible light irradiation, the Au@CdS/MIL-101 heterostructure presents superior hydrogen evolution rate over the pure CdS, CdS/MIL-101 and Au/MIL-101 composites. The Au@CdS/MIL-101 heterostructure exhibits an unusual H<sub>2</sub> production rate of 250 μmol h<sup>-1</sup>/10 mg, which is 2.6 times higher than that of pure CdS. The performance enhancement of Au@CdS/MIL-101 heterostructure can be attributed to the following reasons: (i) the large surface area of MIL-101(Cr) can effectively disperse the Au and CdS nanoparticles, resulting in more active adsorption sites and reaction centers. (ii) the strong surface plasmon resonance absorption of Au could accelerate the charge transfer and extend the light response spectrum of CdS. This three-component Au@CdS/MIL-101 heterostructure combining the large surface area of MOF and the surface plasmon resonance of Au into a single structure may provide a potential way to design highly efficient and solar-energy-harvesting photocatalysts.

© 2015 Elsevier B.V. All rights reserved.

## 1. Introduction

The growing energy and environmental crises call for clean and environmental friendly renewable energy alternatives. Photocatalytic hydrogen evolution from water over semiconductor material has attracted extensive attention because it's a promising way for conversion of solar energy into hydrogen [1–3]. Among various semiconductor materials in present research, CdS has been intensively investigated due to its visible light response (bandgap around 2.4 eV) and the suitable band alignment for water splitting [4,5]. However, there are several inherent drawbacks for pure CdS, such as high photogenerated charge recombination rate. Moreover, the CdS particles are apt to aggregate and form large particles in reaction, resulting in a reduced surface area and decreased photocatalytic performance. Many efforts have been devoted to solve these problems, such as loading different cocatalysts [6–8], coupling CdS with noble metal [9], preparing quantum-sized CdS [10], coupling CdS with other semiconductors [11–14] and hybridizing

CdS with polymers [15,16], etc. Among them, coupling with noble metal nanoparticles (such as Au, Ag) is considered as an effective strategy to enhance the photocatalytic activity of CdS due to the localized surface plasmon resonance [17–21]. The excited electrons on Au nanoparticles through the excitation of localized surface plasmon resonance will inject into the conduction band of CdS, improving the photocatalytic activity. In addition, the location of the noble metal also affects the hydrogen production performance of photocatalysts to a large extent.

Metal-organic frameworks (MOFs) have attracted tremendous interests due to their high surface areas, tunable porosity, crystalline open structures and multifunctionalities [22–24]. Some MOFs have emerged as potential candidates for photocatalysis. Recently, MOFs were reported as popular host matrix for dispersing metal and semiconductor nanoparticles [25–31]. The high surface area of MOFs can well disperse the semiconductor nanoparticles and avoid the aggregation of nanoparticles. And the large surface area of MOFs also can provide more active adsorption sites and photocatalytic reaction centers which would improve the photocatalytic performances. Moreover, the synergistic effect between MOFs and semiconductor can promote the charge separation, enhancing the photocatalytic activity.

\* Corresponding authors. Fax: +86 10 6972 4721.

E-mail addresses: [jianggy@cup.edu.cn](mailto:jianggy@cup.edu.cn) (G. Jiang), [zhenzhao@cup.edu.cn](mailto:zhenzhao@cup.edu.cn) (Z. Zhao).

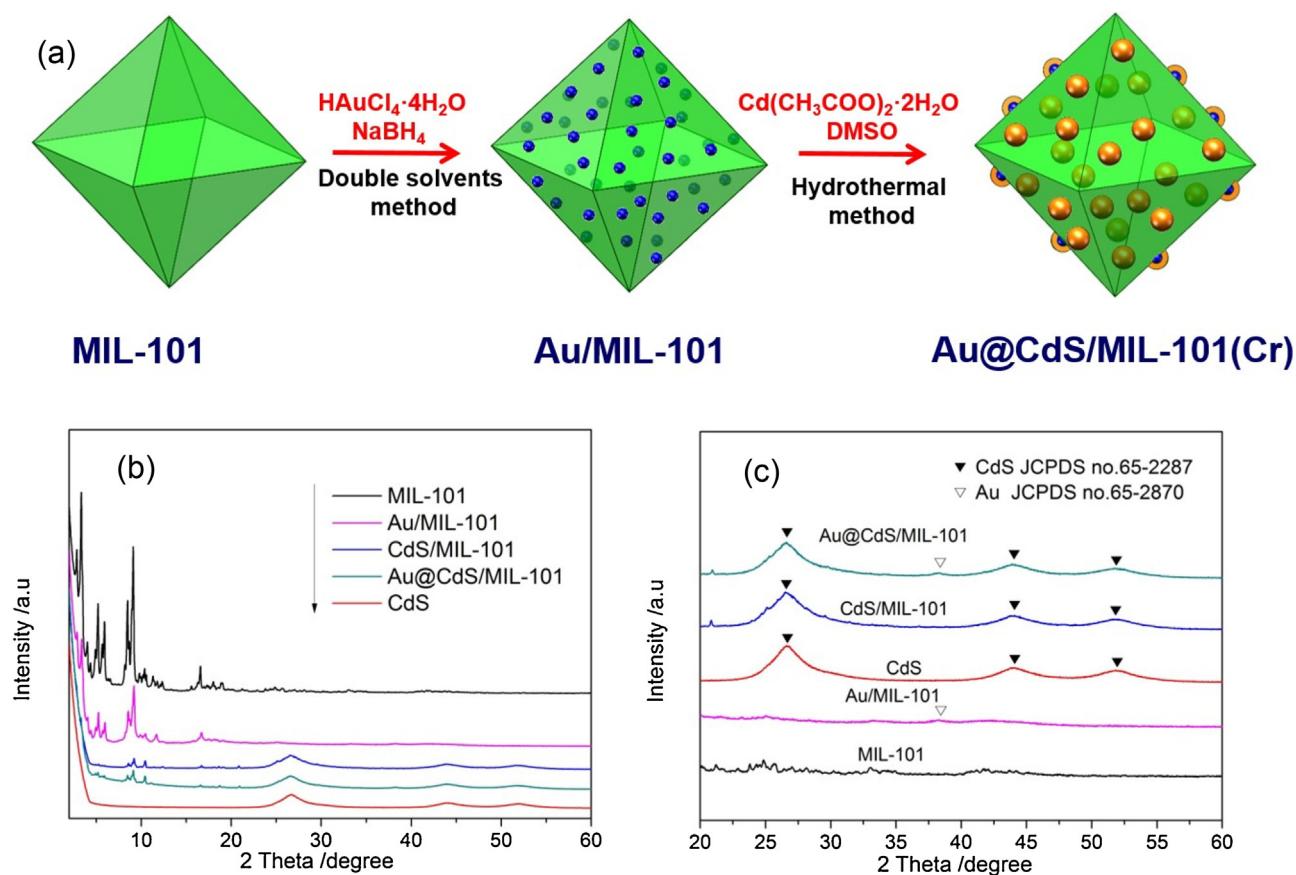


**Fig 1.** (a) Scheme of the preparation process of the Au@CdS/MIL-101 heterostructure, (b) XRD patterns of CdS, MIL-101, CdS/MIL-101, Au/MIL-101 and Au@CdS/MIL-101 heterostructure, (c) the enlarged XRD patterns.

Particularly,  $\text{TiO}_2$ @MOF-5 [30], CdS/MIL-101 [28], rhodamine B sensitized Pt@UiO-66(Zr) [26], reduced graphene oxide/CdS/UiO-66 [27] have been reported. Although several two-component MOFs based composite photocatalysts have been developed, there are few reports about three-component MOFs based heterostructure. Significantly, a three-component heterostructure can greatly enhance photocatalytic activity by introducing a noble metal as a medium which effectively accelerates charge transfer [17–33]. Three-component heterostructure including MOFs and Au nanoparticles could combine the large surface area of MOFs and the surface plasmon resonance of Au into a single structure, which may greatly enhance the photocatalytic activity and extend the light response range of photocatalyst.

Herein, we report the first example of a novel and highly efficient three-component Au@CdS/MIL-101 heterostructure. MIL-101(Cr) is a chromium-based MOFs, which has large surface area, high stability in air, water, common solvents, and thermal treatment [34,35]. Therefore, MIL-101(Cr) was chosen as a stabilizing matrix for the well dispersed growth of Au nanoparticles, then CdS was selectively coated on the Au particles to form Au@CdS core-shell structure. Au@CdS core-shell structure may suppress the formation of  $\text{CdSO}_4$  from CdS [36], which is beneficial for enhancing the stability of CdS. Au nanoparticles serve as sensitizers due to their strong surface plasmon resonance, which can improve the photocatalytic efficiency and extend the light response spectrum of CdS. Moreover, the synergistic effect between MIL-101, Au and CdS can improve the hydrogen evolution performance. Compared with pure CdS, MIL-101, CdS/MIL-101, Au/MIL-101, the Au@CdS/MIL-101 heterostructure exhibits a higher hydrogen evolution rate. The Au@CdS/MIL-101 heterostructure presents an unusual  $\text{H}_2$  produc-

tion rate of  $250 \mu\text{mol} \cdot \text{h}^{-1} / 10 \text{ mg}$ , which is 2.6 times higher than that of pure CdS nanoparticles. The structure and the mechanism of the improved hydrogen evolution performance of the Au@CdS/MIL-101 heterostructure were systematically investigated.

## 2. Experimental

### 2.1. Preparation of Au@CdS/MIL-101 heterostructure

#### Preparation of MIL-101

The MIL-101 was synthesized via a hydrothermal method according to literature [37]. Typically, 0.4 g  $\text{Cr}(\text{NO}_3)_3 \cdot 9\text{H}_2\text{O}$ , 0.05 g fluorhydric acid (40%), 0.164 g 1,4-benzene dicarboxylic acid were added in 4.8 mL  $\text{H}_2\text{O}$  solution. The solution stirred at room temperature for 30 min then the solution was transferred to 23 mL autoclave and maintained at  $220^\circ\text{C}$  for 8 h. After natural cooling, the obtained mixture was filtered several times and dried at  $80^\circ\text{C}$  to get pure MIL-101. Then, the as-prepared MIL-101 was dispersed in 20 mL ethanol and was transferred to 23 mL autoclave. The autoclave was held at  $100^\circ\text{C}$  for 20 h. Finally, after natural cooling, the obtained MIL-101 was washed by ethanol several times and dried at  $150^\circ\text{C}$  for 8 h. Then, the activated MIL-101 was obtained.

#### Preparation of Au/MIL-101

The Au/MIL-101 was synthesized using double solvents method according to literature [38]. Typically, 100 mg of activated MIL-101 was dispersed in 40 mL of dry *n*-hexane. The mixture was sonicated for about 20 min to achieve a homogeneous solution. Then, 60  $\mu\text{L}$   $\text{HAuCl}_4 \cdot 4\text{H}_2\text{O}$  (0.19 mol/L) was added dropwise into the solution while vigorous stirring. After continuously stirred for

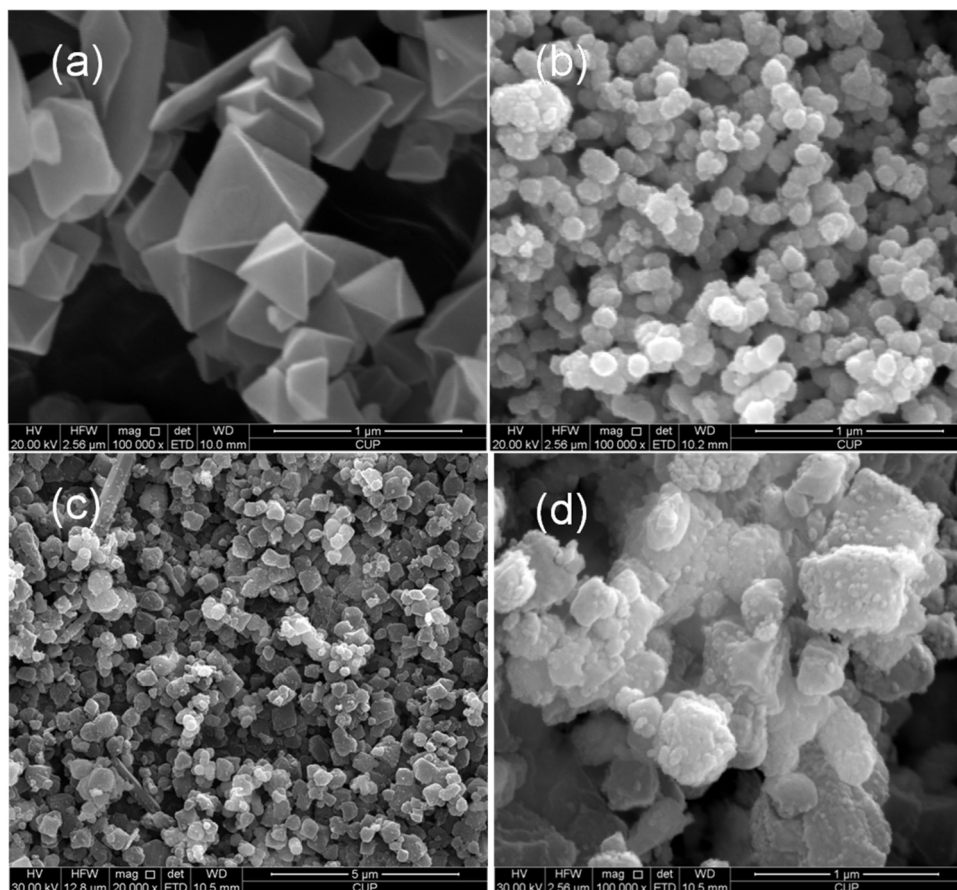


Fig. 2. SEM images of (a) MIL-101, (b) CdS, (c) Au@CdS/MIL-101, (d) enlarged image of Au@CdS/MIL-101.

3 h, the obtained powder was separated from the solution and dried in air at room temperature for 10 h. Then, the  $\text{Au}^{3+}$ /MIL-101 sample was obtained after further dried at  $100^\circ\text{C}$  for 8 h. To reduce  $\text{Au}^{3+}$ /MIL-101 to Au/MIL-101, 5 mL freshly prepared  $\text{NaBH}_4$  (0.6 mol/L) solution was added with vigorous stirring. After continuously stirred for 1 h, the Au/MIL-101 sample was obtained by centrifuging and drying at  $100^\circ\text{C}$ .

#### Preparation of Au@CdS/MIL-101

Typically, 0.04 g of Au/MIL-101 was added into 35 mL of dimethyl sulfoxide (DMSO). After stirred for 10 min, 0.1 g cadmium acetate was added into the above solution and further stirred for 2 h. Then, the solution was transferred to 50 mL autoclave and maintained at  $180^\circ\text{C}$  for 12 h. After natural cooling, the obtained powder was washed by ethanol several times and collected by centrifugation. Then, the powder was added into 40 mL ethanol, then transferred to autoclave and held at  $100^\circ\text{C}$  for 20 h. After natural cooling, the Au@CdS/MIL-101 was washed and dried at  $150^\circ\text{C}$ . For reference, CdS/MIL-101 sample was prepared via the same method without Au.

#### 2.2. Characterization

X-ray diffraction (XRD) patterns were measured by a diffractometer (Shimadzu XRD 6000), using  $\text{Cu K}\alpha$  radiation ( $\lambda = 0.15406 \text{ nm}$ ). The morphologies of the as-prepared samples were observed by scanning electron microscopy (SEM) and transmission electron microscopy (TEM). SEM was performed on a FEI Quanta 200F scanning electron microscope at an accelerating voltage of 30 kV. TEM and HRTEM images were obtained by a FEI Tecnai F20 field emission source electron microscope with an accelerat-

ing voltage of 120 kV. Scanning transmission electron microscopy (STEM) and Energy-dispersive X-ray spectroscopy (EDS) elemental mapping images were also obtained by the FEI F20 electron microscope operating at 150 kV accelerating voltage. UV–vis diffuse reflectance spectroscopy (DRS) was performed on a Hitachi 4100 with the integration sphere diffuse reflectance attachment, and  $\text{BaSO}_4$  was used as the reference. The Brunauer–Emmett–Teller (BET) surface area and pore size distribution were measured by Micromeritics ASAP2010 analyzer.

#### 2.3. Photocatalytic activity measurement

The  $\text{H}_2$  evolution performance of the as-prepared samples were measured under visible light irradiation ( $\lambda > 420 \text{ nm}$ ). A 300 W Xe arc lamp (Beijing perfect-light Co., Ltd.) with a 420 nm cutoff filter was used as the visible light source. Typically, 10 mg photocatalyst was dispersed in a 100 mL water solution containing 20 mmol  $\text{Na}_2\text{S}$  and  $\text{Na}_2\text{SO}_3$ . The amount of evolved  $\text{H}_2$  was measured by a gas chromatograph (GC) equipped with a thermal conductivity detector (TCD). The apparent quantum efficiency (AQE) was measured under the same reaction condition with irradiation light at 420 nm by using band-pass filter, and the AQE was calculated using the following equation:

$$\text{AQE}(\%) = \frac{\text{number of evolved } \text{H}_2 \text{ molecules}}{\text{number of incident photons}} \times 100$$



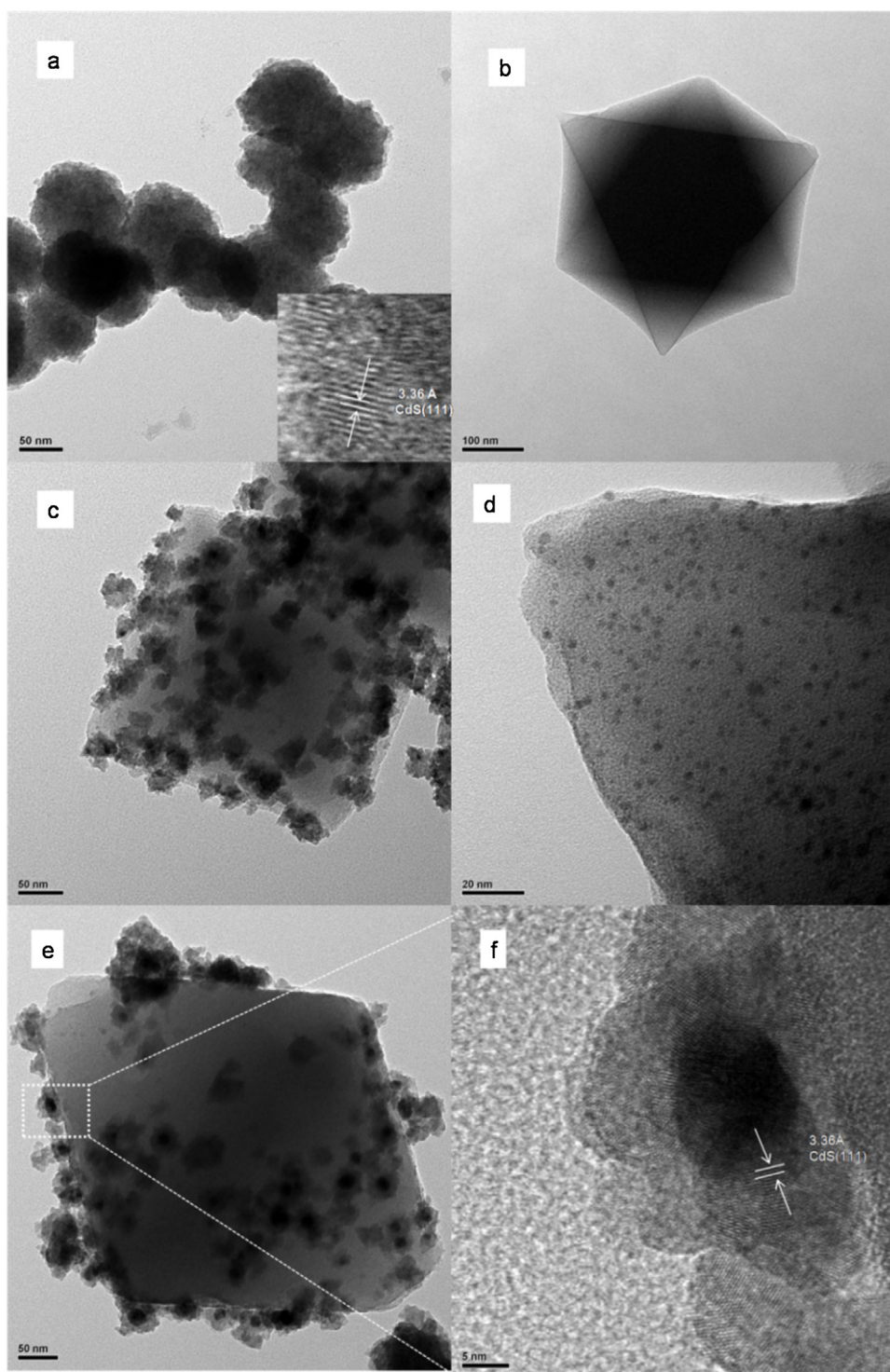


**Fig. 3.** TEM images of (a) CdS, (b) MIL-101, (c) CdS/MIL-101, (d) Au/MIL-101, (e) Au@CdS/MIL-101 and HRTEM image of (f) Au@CdS/MIL-101.

### 3. Results and discussion

#### 3.1. Catalyst characterization

The Au@CdS/MIL-101 heterostructure was prepared using a two-step method and the fabrication process shown in Fig. 1a. Firstly, Au nanoparticles were deposited on the MIL-101 matrix using a double solvents method. Then, CdS shell was selectively coated on the Au particles by a hydrothermal method. Fig. 1(b) and (c) shows the XRD patterns of pure CdS, MIL-101, CdS/MIL-

101, Au/MIL-101 and Au@CdS/MIL-101 heterostructure. For pure MIL-101, the diffraction peaks can be well matched with the simulated MIL-101 reported in the literature [37], proving that MIL-101 was successfully synthesized. For pure CdS, the peaks at  $26.5^\circ$ ,  $43.9^\circ$  and  $52.0^\circ$  are related to (111), (220) and (311) crystal planes of cubic CdS (JCPDS no. 65-2287). The Au@CdS/MIL-101 exhibits the characteristic diffraction peaks of CdS and MIL-101, indicating that the CdS was deposited successfully and the structure of MIL-101 was not changed after Au and CdS modification. Moreover, the peak at  $38.2^\circ$  which corresponds to Au (111) crystal planes

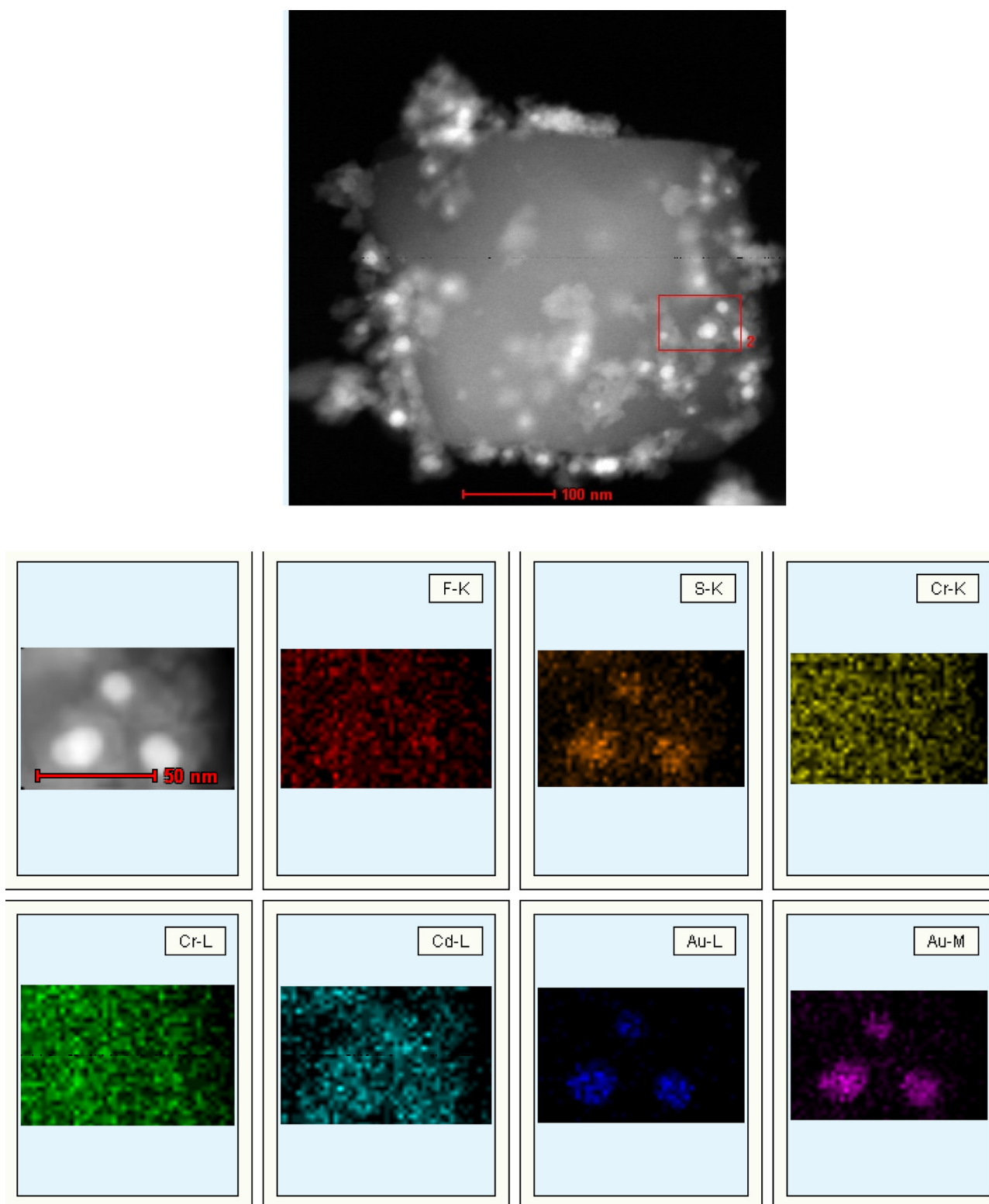


**Fig. 4.** STEM images and elemental mapping images of Au@CdS/MIL-101 heterostructure.

can be observed in Au@CdS/MIL-101 and Au/MIL-101 composite (Fig. 1c) (JCPDS no. 65-2870), demonstrating the existence of Au. As can be seen, a three-component Au@CdS/MIL-101 heterostructure was successfully synthesized. The morphology of MIL-101, CdS and Au@CdS/MIL-101 were shown in Fig. 2. As can be seen from Fig. 2a, the as-prepared MIL-101 displays octahedral nanocrystals with smooth surface, and the sizes of MIL-101 are in the range of

300–500 nm. As shown in Fig. 2b, the sizes of pure CdS particles are about 100 nm. After deposited with Au@CdS core shell particles, the surface of the MIL-101 become rough and no significant change of the morphology of MIL-101 can be observed. The Au@CdS nanoparticles with average size of 50 nm are well dispersed on the surface of MIL-101 matrix without obvious aggregation. It is worth to point out that MIL-101 effectively inhibit the growth of CdS particles and

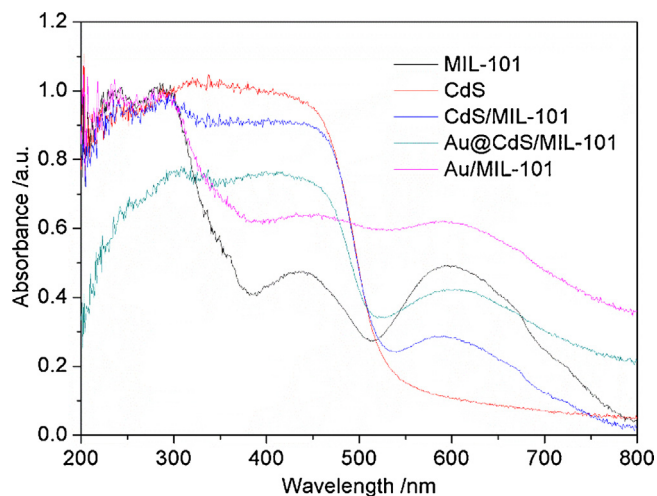


Fig. 5. UV-vis DRS spectra of CdS, MIL-101, Au/MIL-101, CdS/MIL-101 and Au@CdS/MIL-101 heterostructure.

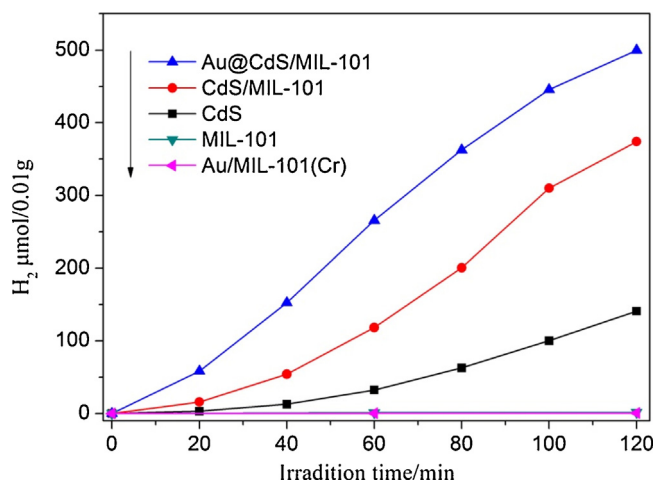


Fig. 6. Hydrogen evolution profiles of CdS, MIL-101, Au/MIL-101, CdS/MIL-101 and Au@CdS/MIL-101 under visible-light illumination over 100 mL aqueous solution containing 10 mg photocatalysts and 20 mmol Na<sub>2</sub>S and Na<sub>2</sub>SO<sub>3</sub> as sacrificial reagents; 300 W Xe arc lamp with a UV-cutoff filter ( $\geq 420$  nm) used as the visible-light source.

the aggregation phenomenon of CdS. Furthermore, the CdS/MIL-101 samples of different MIL-101 proportion (20%–80%) were also investigated and the SEM images are shown in Fig. S1. As can be seen, in all CdS/MIL-101 samples, the CdS particles are uniformly deposited on the MIL-101 surface without obvious aggregation. The CdS of CdS/MIL-101(40%) sample has the optimal dispersion state, so proportion of MIL-101 is determined to be 40% in the following experiment.

TEM and HRTEM measurements were carried out to further characterize the morphology of CdS, MIL-101 and Au@CdS/MIL-101 heterostructure (Fig. 3). The CdS particles show an average diameter of about 100 nm, and the measured interplanar spacing of CdS is 3.36 Å, which is related to the CdS (111) plane [18] (Fig. 3a). The MIL-101 shows a typical octahedral structure with an average size of 400 nm. The TEM images of CdS/MIL-101 and Au/MIL-101 sample were also investigated for comparison. In the CdS/MIL-101 sample, CdS particles with the diameter of 25 nm are well dispersed on the surface of MIL-101. Similarly, Au particles with the diameter of 7 nm are also highly dispersed on the surface of MIL-101 (Fig. 3d and f) without any obvious aggregation, indicating that the MIL-101 is a good matrix for well-dispersed growth of CdS and Au particles.

As can be seen from the HRTEM image of Au@CdS/MIL-101 heterostructure (Fig. 3e, Fig.S2), core-shell particles are well dispersed on the surface of MIL-101, and the average diameter of the core-shell particles were similarly with that on CdS/MIL-101 sample. The core and shell show different contrast in HRTEM image, and the marked lattice spacing of 3.36 Å on the shell is corresponded to the (111) plane of CdS. These results suggest that an intimate contact was formed between CdS, Au and MIL-101, and this contact may be helpful for the charge separation and transfer.

The component and structure of Au@CdS core-shell particles were further confirmed by the energy dispersive X-ray spectroscopy (EDS) (Fig. 4). The uniform F, Cr elements in the background are indexed to the MIL-101 matrix. The core-shell particles are composed of Au, S, Cd, and the Au signals are mainly confined within the Au core region, while a high intensity of S and Cd are found in the shell area. These results indicate that the CdS are selectively coated on the surface of Au particles and the Au@CdS/MIL-101 heterostructure is successfully constructed. This is well along with the Au@CdS/MIL-101 configuration observed in the TEM image (Fig. 3e and f, Fig.S2), and the selective deposition of CdS ensures the efficient photogenerated charge separation and transfer.

UV-vis DRS spectra were used to analyze the optical properties of the MIL-101 and the as-prepared samples (Fig. 5). MIL-101 exhibits two characteristic absorption band centered at 450 nm and 600 nm, which coincides with that in literature [28]. The band of pure MIL-101 in the UV region belongs to  $\pi-\pi^*$  transitions of ligands and the bands in the visible region can be assigned to the d-d spin-allowed transition of the Cr<sup>3+</sup> [28]. CdS displays a sharp fundamental absorption edge rise at 530 nm as expected, corresponding to a band gap of 2.3 eV. Compared with that of MIL-101, the Au/MIL-101 shows an enhanced broad absorption in visible light region, this may correspond to the plasmon resonance absorption of Au nanoparticles. Compared with that of pure CdS, the CdS/MIL-101 composite shows an adsorption band centered at 600 nm, which is attributed to the absorption of MIL-101 matrix. The absorbance spectrum of Au@CdS/MIL-101 shows a combination of the spectral features of pure CdS, Au and MIL-101, and it exhibits a sharp absorption edge rise at about 520 nm and a broad absorption in visible light region. These results demonstrate that the modification of Au and MIL-101 effectively extends the light absorption range of CdS, which may be beneficial for the visible light utilization and photocatalytic reaction.

To investigate the specific surface area and porosity of the as-prepared samples, nitrogen adsorption-desorption measurement was carried out, and the results are shown in Fig. S3. The pure MIL-101 shows a typical I isotherm indicating the micropore characteristics as described in the literature [37]. The Au/MIL-101, CdS/MIL-101 and Au@CdS/MIL-101 also display typical type I isotherms. The BET surface area, pore volume and adsorption capacity of the as-prepared samples are listed in Table S1. The BET surface area, pore volume and adsorption capacity of MIL-101 are measured as 2873.0 m<sup>2</sup>/g, 1.42 cm<sup>3</sup>/g and 921.2 cm<sup>3</sup>/g. BET surface area is decreased step-by-step from MIL-101, Au/MIL-101, CdS/MIL-101 and Au@CdS/MIL-101. After deposited with Au and CdS, the BET surface area of MIL-101 decreases from 2873.0 m<sup>2</sup>/g to 223.9 m<sup>2</sup>/g, which indirectly indicates that the Au and CdS are successfully deposited on the MIL-101 matrix. Nevertheless, the surface area of Au@CdS/MIL-101 is still much larger than that of pure CdS. These results also demonstrate that Au@CdS/MIL-101 heterostructure still maintain the porous structure and relative large surface area of MIL-101, and the high surface area can provide more adsorption and reaction active sites for the photocatalytic reaction.



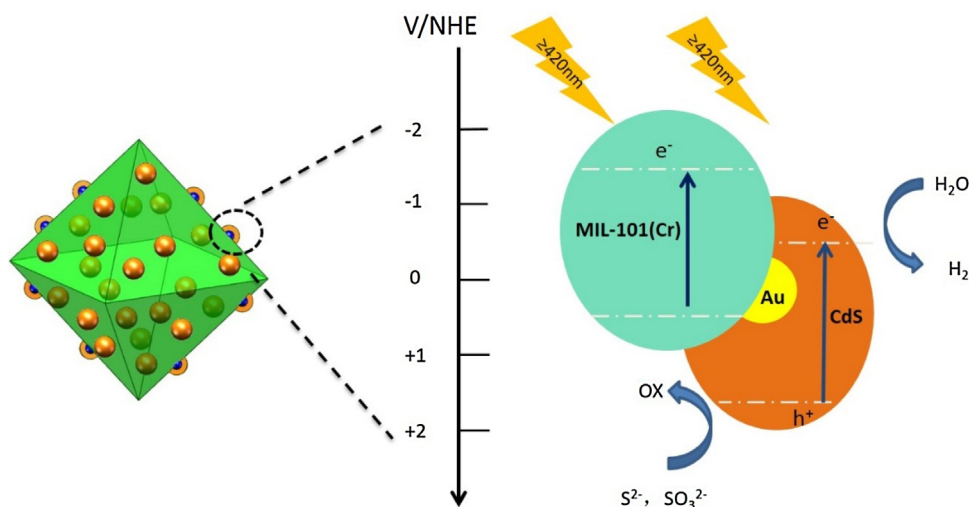


Fig. 7. Schematic of the energy band structure of the Au@CdS/MIL-101 heterostructure.

### 3.2. Hydrogen evolution performance

The photocatalytic  $\text{H}_2$  evolution of as-prepared samples was evaluated in  $\text{Na}_2\text{S}$  and  $\text{Na}_2\text{SO}_3$  aqueous solution under visible light irradiation. To get the optimal MIL-101 proportion, the photocatalytic  $\text{H}_2$  evolution performance of various CdS/MIL-101 samples with different MIL-101 proportion (20%–80%) were investigated and the results were shown in Fig.S4. The  $\text{H}_2$  production rate of CdS, CdS/MIL-101(20%), CdS/MIL-101(40%), CdS/MIL-101(60%), CdS/MIL-101(80%) are  $70.4 \mu\text{mol h}^{-1}/10 \text{ mg}$ ,  $152.3 \mu\text{mol h}^{-1}/10 \text{ mg}$ ,  $187.1 \mu\text{mol h}^{-1}/10 \text{ mg}$ ,  $208.2 \mu\text{mol h}^{-1}/10 \text{ mg}$ ,  $152.3 \mu\text{mol h}^{-1}/10 \text{ mg}$ , respectively. The photocatalytic  $\text{H}_2$  evolution rate of CdS/MIL-101 first increases then decreases with the increase of the MIL-101 proportion, and all CdS/MIL-101 composites show higher  $\text{H}_2$  production rate than pure CdS. Combined with the SEM results, the proportion of MIL-101 is determined to be 40% in the following experiment.

The photocatalytic  $\text{H}_2$  evolution of CdS, Au/MIL-101, CdS/MIL-101 and Au@CdS/MIL-101 was evaluated under visible light irradiation ( $\lambda \geq 420 \text{ nm}$ ) and the results were shown in Fig. 6. There is no appreciable  $\text{H}_2$  evolution can be detected in the absence of photocatalyst or the light irradiation. Moreover, no appreciable  $\text{H}_2$  evolution was detected over MIL-101 and Au/MIL-101, suggesting that MIL-101 has no photocatalytic  $\text{H}_2$  production activity. As can be seen, all of the CdS composites display higher photocatalytic  $\text{H}_2$  evolution activity than that of pure CdS. The  $\text{H}_2$  evolution activity rate is enhanced step-by-step from pure CdS, CdS/MIL-101 to Au@CdS/MIL-101 heterostructure. The Au@CdS/MIL-101 heterostructure presents an unusual  $\text{H}_2$  production rate of  $250.0 \mu\text{mol h}^{-1}/10 \text{ mg}$ , which is 2.6 times higher than that of pure CdS nanoparticles ( $70.4 \mu\text{mol h}^{-1}/10 \text{ mg}$ ). The quantum efficiency for the photocatalytic  $\text{H}_2$  evolution over Au@CdS/MIL-101 heterostructure was determined to be 8.8% at 420 nm. These results demonstrate that the introduction of Au and MIL-101 can effectively increase the  $\text{H}_2$  evolution performance of CdS. To investigate the effect of MIL-101 in charge separation and transfer process, Au@CdS deposited in an inactive support ( $\text{SiO}_2$ ) was synthesized. And Au directly deposited on CdS was also synthesized as reference. The  $\text{H}_2$  evolution performance of as-prepared samples was shown in Fig.S5. As can be seen, the Au@CdS/MIL-101 displays higher photocatalytic  $\text{H}_2$  evolution activity than Au/CdS and Au/CdS/ $\text{SiO}_2$ , indicating that the existence of MIL-101 can effectively enhance the photocatalytic performance. Moreover, the  $\text{H}_2$  evolution rate of Au@CdS/MIL-101 heterostructure is higher than

that of CdS/MIL-101, indicating that the introduction of Au can accelerate the charge transfer between CdS and MIL-101, thus enhancing the  $\text{H}_2$  evolution performance. The Au nanoparticles can serve as sensitizers due to the strong surface plasmon resonance, which can extend the light response range of CdS.

To estimate the stability of Au@CdS/MIL-101 heterostructure, the recycled experiments for  $\text{H}_2$  production from water were performed, and the results were shown in Fig. S6. At the end of each run, the reaction cell was vacuumed for 30 min to remove the produced  $\text{H}_2$ . As can be seen, the Au@CdS/MIL-101 heterostructure shows considerable durability in four consecutive runs. These results indicate that the Au@CdS/MIL-101 heterostructure has good stability in  $\text{H}_2$  production from water.

### 3.3. Mechanism of enhancement of photocatalytic performance

On the basis of above results, a possible mechanism for the high  $\text{H}_2$  production performance and efficient electron-hole separation at the Au@CdS/MIL-101 heterostructure is proposed in Fig. 7. Under the visible light irradiation, CdS is excited to generate electrons in the conduction band (CB) and holes in the valence band (VB). The redox potential ( $\text{Cr}^{3+}/\text{Cr}^{2+}$ ) of MIL-101 is +0.49 V, and the reduction potential of MIL-101 is  $-1.57 \text{ V}$  [28]. MIL-101 could absorb visible light to induce MIL-101( $\text{Cr}^{\text{III}}$ )-MIL-101( $\text{Cr}^{\text{IV}}$ ) transition [35]. There are two possible electron transfer paths in Au@CdS/MIL-101 heterostructure: (i) the excited electrons of MIL-101( $\text{Cr}^{\text{IV}}$ ) would transfer to the CB of CdS due to the well matched energy level (as shown in Fig. 7) [5,28,39]. The excited electrons of CdS will react with the  $\text{H}^+$  ions to produce  $\text{H}_2$ . (ii) the excited electrons of MIL-101( $\text{Cr}^{\text{IV}}$ ) transfer to Au, then the electrons in Au will subsequently transfer to CdS. The surface plasmon response of Au could accelerate the electron transfer from the MIL-101 to the CB of CdS, enhancing the sensitization effect of CdS by MIL-101. The electron of CdS will react with the  $\text{H}^+$  ions to produce  $\text{H}_2$ , whereas the holes in the VB of CdS will be trapped by the sacrificial reagents ( $\text{Na}_2\text{S}$  and  $\text{NaSO}_3$ ). Therefore, the improvement of  $\text{H}_2$  evolution performance of Au@CdS/MIL-101 heterostructure can be ascribed to the following reasons: (i) the large specific surface area of MIL-101 can effectively disperse the Au and CdS nanoparticles, which could provide more active adsorption sites and reaction centers. Meanwhile, the small size and well dispersion of CdS nanoparticles on Au@CdS/MIL-101 heterostructure can improve the charge separation and photocatalytic activity. Moreover, the MIL-101 not only serves as a support, but also acts as a photo-electron generator to

improve the photocatalytic activity. (ii) the strong surface plasmon resonance absorption of Au could accelerate the charge transfer and extend the response spectrum of CdS.

#### 4. Conclusions

Au@CdS/MIL-101 heterostructure was successfully prepared via a facile two-step method. Au nanoparticles were well-dispersed on the MIL-101 matrix by double solution method, and then CdS was selectively coated on the Au nanoparticles. The good dispersion of CdS and Au nanoparticles, as well as the strong surface plasmon resonance absorption of Au lead to an accelerated electron separation and transfer. Under visible light irradiation, the Au@CdS/MIL-101 heterostructure presents an unusual H<sub>2</sub> production rate of 250  $\mu\text{mol h}^{-1}$ /10 mg, which is 2.6 times higher than that of pure CdS. The present result may provide a new way to fabricate novel and highly efficient MOF based heterostructure photocatalysts.

#### Acknowledgements

This work is supported by the National Science Foundation of China (Grant No. U1162117, 21307020), Beijing Nova Program (Grant No. Z11111005450000), Prospect Oriented Foundation of China University of Petroleum, Beijing (Grant No. ZX20140257), Beijing Higher Education Young Elite Teacher Project (YETP0696), National Basic Research Program of China (973 Program, No. 2012CB215001), Beijing Natural Science Foundation (Grant No. 2144059) and Science Foundation of China University of Petroleum, Beijing (Grant No. 2462014YJRC010).

#### Appendix A. Supplementary data

Supplementary data associated with this article can be found, in the online version, at <http://dx.doi.org/10.1016/j.apcatb.2015.12.020>.

#### References

- [1] X. Chen, S. Shen, L. Guo, S.S. Mao, *Chem. Rev.* 110 (2010) 6503–6570.
- [2] A. Kudo, Y. Miseki, *Chem. Soc. Rev.* 38 (2009) 253–278.
- [3] H. Wang, L. Zhang, Z. Chen, J. Hu, S. Li, Z. Wang, J. Liu, X. Wang, *Chem. Soc. Rev.* 43 (2014) 5234–5244.
- [4] Y. Yin, Z. Jin, F. Hou, *Nanotechnology* 18 (2007) 495608.
- [5] Y. Wang, F. Wang, J. He, *Nanoscale* 5 (2013) 11291–11297.
- [6] X. Zong, H. Yan, G. Wu, G. Ma, F. Wen, L. Wang, C. Li, *J. Am. Chem. Soc.* 130 (2008) 7176–7177.
- [7] X. Zong, G. Wu, H. Yan, G. Ma, J. Shi, F. Wen, L. Wang, C. Li, *J. Phys. Chem. C* 114 (2010) 1963–1968.
- [8] X. Zong, J. Han, G. Ma, H. Yan, G. Wu, C. Li, *J. Phys. Chem. C* 115 (2011) 12202–12208.
- [9] N. Zhang, S. Liu, Y.J. Xu, *Nanoscale* 4 (2012) 2227–2238.
- [10] A.J. Hoffman, G. Mills, H. Yee, M.R. Hoffmann, *J. Phys. Chem.* 96 (1992) 5546–5552.
- [11] H. Park, W. Choi, M.R. Hoffmann, *J. Mater. Chem.* 18 (2008) 2379.
- [12] Y. Tak, S.J. Hong, J.S. Lee, K. Yong, *J. Mater. Chem.* 19 (2009) 5945–5951.
- [13] X. Wang, G. Liu, Z.-G. Chen, F. Li, L. Wang, G.Q. Lu, H.M. Cheng, *Chem. Commun.* (2009) 3452–3454.
- [14] L. Ge, F. Zuo, J. Liu, Q. Ma, C. Wang, D. Sun, L. Bartels, P. Feng, *J. Phys. Chem. C* 116 (2012) 13708–13714.
- [15] H. Zhang, Y. Zhu, *J. Phys. Chem. C* 114 (2010) 5822–5826.
- [16] K. He, M. Li, L. Guo, *Int. J. Hydrogen Energ.* 37 (2012) 755–759.
- [17] Z.B. Yu, Y.P. Xie, G. Liu, G.Q. Lu, X.L. Ma, H.M. Cheng, *J. Mater. Chem. A* 1 (2013) 2773–2776.
- [18] X. Cui, Y. Wang, G. Jiang, Z. Zhao, C. Xu, Y. Wei, A. Duan, J. Liu, J. Gao, *RSC Adv.* 4 (2014) 15689–15694.
- [19] K. Xie, Q. Wu, Y. Wang, W. Guo, M. Wang, L. Sun, C. Lin, *Electrochem. Commun.* 13 (2011) 1469–1472.
- [20] L. Ding, H. Zhou, S. Lou, J. Ding, D. Zhang, H. Zhu, T. Fan, *Int. J. Hydrogen Energ.* 38 (2013) 8244–8253.
- [21] H. Tada, T. Mitsui, T. Kiyonaga, T. Akita, K. Tanaka, *Nat. Mater.* 5 (2006) 782–786.
- [22] K.G. Laurier, F. Vermoortele, R. Ameloot, D.E. De Vos, J. Hofkens, M.B. Roeffaers, *J. Am. Chem. Soc.* 135 (2013) 14488–14491.
- [23] P. Serra-Crespo, E.V. Ramos-Fernandez, J. Gascon, F. Kapteijn, *Chem. Mater.* 23 (2011) 2565–2572.
- [24] A. Clough, S.T. Zheng, X. Zhao, Q. Lin, P. Feng, X. Bu, *Cryst. Growth. Des.* 14 (2014) 897–900.
- [25] Y.P. Yuan, L.S. Yin, S.W. Cao, G.S. Xu, C.H. Li, C. Xue, *Appl. Catal. B-Environ.* 168–169 (2015) 572–576.
- [26] J. He, J. Wang, Y. Chen, J. Zhang, D. Duan, Y. Wang, Z. Yan, *Chem. Commun.* 50 (2014) 7063–7066.
- [27] R. Lin, L. Shen, Z. Ren, W. Wu, Y. Tan, H. Fu, J. Zhang, L. Wu, *Chem. Commun.* 50 (2014) 8533–8535.
- [28] J. He, Z. Yan, J. Wang, J. Xie, L. Jiang, Y. Shi, F. Yuan, F. Yu, Y. Sun, *Chem. Commun.* 49 (2013) 6761–6763.
- [29] F. Ke, L. Wang, J. Zhu, *Nanoscale* 7 (2015) 1201–1208.
- [30] M. Muller, X. Zhang, Y. Wang, R.A. Fischer, *Chem. Commun.* (2009) 119–121.
- [31] L. Shen, M. Luo, Y. Liu, R. Liang, F. Jing, L. Wu, *Appl. Catal. B-Environ.* 166–167 (2015) 445–453.
- [32] H. Zhu, B. Yang, J. Xu, Z. Fu, M. Wen, T. Guo, S. Fu, J. Zuo, S. Zhang, *Appl. Catal. B-Environ.* 90 (2009) 463–469.
- [33] H.J. Yun, H. Lee, N.D. Kim, D.M. Lee, S. Yu, J. Yi, *ACS Nano* 5 (2011) 4084–4090.
- [34] A. Aijaz, T. Akita, N. Tsumori, Q. Xu, *J. Am. Chem. Soc.* 135 (2013) 16356–16359.
- [35] M. Wen, K. Mori, T. Kamegawa, H. Yamashita, *Chem. Commun.* 50 (2014) 11645–11648.
- [36] M. Kim, Y.K. Kim, S.K. Lim, S. Kim, S.I. In, *Appl. Catal. B-Environ.* 166–167 (2015) 423–431.
- [37] G. Ferey, C. Mellot-Draznieks, C. Serre, F. Millange, J. Dutour, S. Surble, I. Margiolaki, *Science* 309 (2005) 2040–2042.
- [38] Q.L. Zhu, J. Li, Q. Xu, *J. Am. Chem. Soc.* 135 (2013) 10210–10213.
- [39] Y. Wang, Q. Wang, X. Zhan, F. Wang, M. Safdar, J. He, *Nanoscale* 5 (2013) 8326–8339.